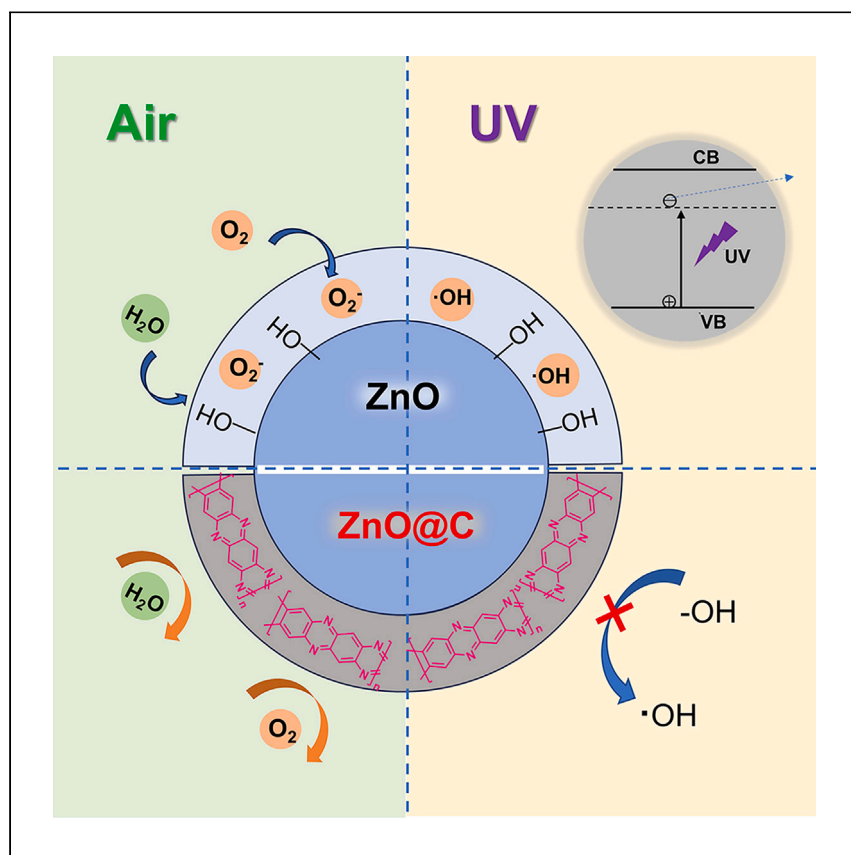


Article

Simultaneous UV and air stability improvement of organic solar cells enabled by carbon-coated zinc oxide as cathode buffer layer



Lingpeng Yan, Yu Wang,
Wensheng Zhao, ..., Qingmei
Su, Hua Wang, Chang-Qi Ma

yanlingpeng@tyut.edu.cn (L.Y.)
yyztyut@126.com (Y.Y.)
cqma2011@sinano.ac.cn (C.-Q.M.)

Highlights

Carbon-coated ZnO quantum dots are synthesized and served as the ETL of OSCs

ZnO@C ETL shows better matching energy levels and improves the PCE of OSCs

ZnO@C NP-based OSCs exhibit significantly enhanced air and UV stability

High UV and air stability are critical for the future application of organic solar cells (OSCs) in architectural integration and outer space. Yan et al. report carbon-coated zinc oxide as electron transporting layers for OSCs, which can significantly improve both their power conversion efficiency and air/UV stability.

Yan et al., Cell Reports Physical Science 4,
101654
November 15, 2023 © 2023 The Authors.
<https://doi.org/10.1016/j.xcrp.2023.101654>



Article

Simultaneous UV and air stability improvement of organic solar cells enabled by carbon-coated zinc oxide as cathode buffer layer

Lingpeng Yan,^{1,2,8,*} Yu Wang,¹ Wensheng Zhao,^{3,4} Han Zha,^{1,4} Haitao Song,^{3,4} Haotian Hao,³ Yelin Hao,¹ Qun Luo,⁴ Feng Liu,⁵ Yongzhen Yang,^{2,3,*} Qingmei Su,^{2,6} Hua Wang,^{3,7} and Chang-Qi Ma^{4,*}

SUMMARY

Zinc oxide nanoparticles (ZnO NPs) are ideal electron transport materials for current high-efficiency organic solar cells (OSCs), but they still face several challenges due to their surface defects and catalytic characteristics. Herein, to address the shortcomings of ZnO NPs, carbon-coated ZnO nanoparticles (ZnO@C NPs) are synthesized. With high hydrophobicity and excellent UV absorption capacity, the thin carbon shell coated on the ZnO NPs can effectively passivate their surface defects, isolate the adsorption of water and oxygen, and inhibit the formation of hydroxyl radicals. Ultimately, the ZnO@C-based PM6:L8-BO OSCs achieve a power conversion efficiency of 17.55%, higher than that of ZnO-based devices (16.92%). What's important, the ZnO@C NP-based OSCs show significantly enhanced air and UV stability. This work highlights the great potential of ZnO@C NPs in fabricating highly efficient, air-stable, and photo-stable OSCs.

INTRODUCTION

Organic solar cells (OSCs) are attracting great attention for their lightness and flexibility, roll-to-roll printability, and the application prospect of architectural integration and outer space.¹ Achieving high power conversion efficiency (PCE) and long operating life are prerequisites for their commercialization. Nowadays, with the breakthrough of nonfullerene acceptors (NFAs), the PCE of OSCs has surpassed 19%,² which is enough for commercial applications. However, the stability and especially the illumination and air stability of OSCs are far from the demand. Although some reports indicated that the intrinsic operational lifetime of OSCs has the potential to approach 10 years or even longer,^{3,4} some studies have demonstrated that the degradation of OSCs can be significantly accelerated by UV light from sunlight as well as water and oxygen in the atmosphere,^{5,6} especially for the NFA-based OSCs. High UV and air stability are critical for the future application of OSCs in architectural integration and outer space; therefore it is imperative to overcome these challenges. Among many strategies for improving the stability of OSCs, interface engineering has always played a crucial role.^{7–10}

Zinc oxide nanoparticles (ZnO NPs) are currently a commonly used electron transporting layer (ETL) material in highly efficient inverted OSCs due to their wide band gap, good electron transport capability, easy preparation, and low-temperature solution processability,^{11,12} but accompanied by a most fatal drawback is that

¹College of Materials Science and Engineering, Taiyuan University of Technology, Taiyuan 030024, China

²Shanxi-Zheda Institute of Advanced Materials and Chemical Engineering, Taiyuan 030032, China

³Key Laboratory of Interface Science and Engineering in Advanced Materials, Ministry of Education, Taiyuan University of Technology, Taiyuan 030024, China

⁴i-Lab & Printable Electronics Research Center, Suzhou Institute of Nano-Tech and Nano-Bionics, Chinese Academy of Sciences, Suzhou 215123, China

⁵School of Energy and Power Engineering, North University of China, Taiyuan 030051, China

⁶Materials Institute of Atomic and Molecular Science, Shaanxi University of Science and Technology, Xi'an 710021, China

⁷College of Textile Engineering, Taiyuan University of Technology, Yuci 030600, China

⁸Lead contact

*Correspondence: yanlingpeng@tyut.edu.cn (L.Y.), yyzytut@126.com (Y.Y.), cqma2011@sinano.ac.cn (C.-Q.M.)
<https://doi.org/10.1016/j.xcrp.2023.101654>



they can photocatalyze the NFA of OSCs to induce device failure.¹³ This catalytic reaction will be aggravated when exposed to UV light, which seriously affects the UV stability of OSCs and ultimately limits their outer space applications. Meanwhile, the numerous hydroxyl defects outside ZnO NPs can generate severe self-aggregation, which is not conducive to the large-scale preparation of OSCs.^{14–16} Furthermore, the hydroxyl defects can also form numerous recombination centers on the surface of ZnO NPs, which leads to poor charge transport and extraction, ultimately increasing the series resistance of OSCs.^{17,18}

In view of this, various strategies to suppress the surface defects of ZnO ETL were proposed, which can be classified into two categories. One is surface modification by polar solvents^{19,20} or small molecules^{21,22} to remove the surface defects. The other is depositing a new interfacial layer on the top of ZnO films to passivate their defects.^{3,23,24} Although these approaches can suppress the surface defects of the ZnO ETL to a certain extent, these modifications mainly act on the surface of the ZnO ETL, thus leading to insufficient passivation. Therefore, a strategy for directly modifying ZnO NPs has been proposed. Wei et al. capped ZnO NPs with a 3-(aminopropyl)trimethoxysilane (ZnO@APTMS NPs) for OSCs, which reduces their surface defects, thus suppressing the light-soaking effect of OSCs. What's important is that the ZnO@APTMS NPs show better dispensability in solvents and air storage stability.¹⁶ Guo et al. used 2-(2-methoxyethoxy) acetic acid to remove the surface hydroxy groups of ZnO NPs, which significantly improve the monodispersed ink stability and thickness independent of ZnO NPs, further enhancing the long-term stability of OSCs.¹⁵ The above studies provide ample evidence that modification of ZnO NPs is a straightforward, effective, and thorough potential strategy to improve the stability of ZnO NPs and OSCs based on a ZnO ETL. However, although effective improvements in the light stability of ZnO-based OSCs have been reported, there are few reports that can effectively inhibit the rapid aging of OSCs caused by the catalysis of ZnO under strong UV light.

With excellent optoelectronic properties, tunable energy level structures, and stable physical and chemical properties,²⁵ carbon nanomaterials have been reported as ETL materials or as ETL modifiers of OSCs.^{25,26} In addition, they exhibit a strong UV absorption capacity and are expected to be promising in solving the UV stability problem of OSCs. Herein, ZnO@C NPs were creatively designed and synthesized by a two-step method using ZnO NPs as core and *o*-phenylenediamine as carbon source. The *o*-phenylenediamine was selected as a carbon source molecule, mainly considering the following reasons. Firstly, the amino group of *o*-phenylenediamine can form hydrogen bonds and coordination bonds with ZnO NPs. Secondly, *o*-phenylenediamine is easy to self-polymerize to form poly(*o*-phenylenediamine) with excellent electrical conductivity.²⁷ Thus, the further carbonization of poly(*o*-phenylenediamine) is beneficial to obtain carbon shells with high electrical conductivity. As expected, the synthesized ZnO@C NPs exhibited better monodispersity, enhanced hydrophobicity, fewer surface defects, and inhibited catalytic properties. Utilizing ZnO@C NPs as the ETL significantly improves the PCE and UV/air stability of OSCs. Overall, this work provides an effective strategy for developing the OSCs of high performance and high air and UV stability.

RESULTS AND DISCUSSION

Morphology and structure of ZnO@C NPs

The synthesis of ZnO@C NPs is a two-stage process (Figure 1). Firstly, ZnO NPs were synthesized by particle precipitation method.²⁸ Then, the methanolic solution of ZnO NPs and different contents of *o*-phenylenediamine (carbon source precursors)



Figure 1. Synthetic process of the ZnO@C NPs

were evenly mixed and further placed in an autoclave by solvothermal method to finally generate ZnO@C NPs (see section “Synthesis of ZnO@C NPs”). In order to clarify the structure and formation mechanism of ZnO@C NPs, the microscopic morphology, crystalline properties, and surface structure of ZnO NPs and ZnO@C NPs have been characterized and compared.

The microscopic morphology of ZnO@C NPs was characterized by transmission electron microscopy (TEM) (Figures 2A–2C and S1). Compared with ZnO NPs, the monodispersity of ZnO@C NPs based on different ratios of *o*-phenylenediamine is improved, with the best dispersion being ZnO@C NPs-30% (*o*-phenylenediamine: 30%). The particle size of ZnO NPs is in the range of 3–5 nm with an average size of 4.54 nm, while the particle sizes of ZnO@C NPs (*o*-phenylenediamine: 10%–80%) are in the range of 5–8 nm with average sizes of 6.40, 6.57, 6.90, and 6.96 nm, respectively. It is clear that the thickness of carbon shell increases with increasing *o*-phenylenediamine content. The best dispersed ZnO@C-30% NPs are further preferentially selected for magnified observation (Figures 2B and 2C). Lattice stripes with a lattice spacing of 0.25 nm are observed in ZnO NPs (Figure 2A) and ZnO@C NPs (Figure 2C), which are attributed to the (101) crystal plane of ZnO.²⁹ An amorphous carbon layer is encapsulated outside the ZnO NPs with a thickness of about 1 nm (Figure 2C). The HR-TEM results visually confirm the generation of the core-shell structure of ZnO@C NPs.

The crystal structure of ZnO@C NPs was analyzed by X-ray diffraction (XRD). As seen in Figure 2D, the diffraction peaks located at 2θ of 31.8°, 34.4°, 36.3°, 47.5°, 56.6°, 62.9°, and 68.0° are detected for ZnO and ZnO@C-30% NPs, corresponding to the (100), (002), (101), (102), (110), (103), and (112) crystal planes of hexagonal ZnO.³⁰ Interestingly, the full width at half maxima of the ZnO@C NPs diffraction peaks is significantly narrower, which implies an increase in the crystallization properties of ZnO NPs. Our preliminary experiments revealed that ZnO NPs continue to grow during solvothermal reactions at high temperatures and pressures. So, when the ZnO NPs are encapsulated by a carbon shell, the formation of the carbon shell layer restricts the growth of ZnO crystals. The carbon shell layer acts as a barrier on the surface of ZnO crystals, preventing further crystal growth and diffusion of crystal facets. During the crystal growth process, the presence of the carbon shell layer inhibits the formation of defects within the crystal, thereby reducing the structural impurities and defect density within the crystal.³¹

The elemental composition and chemical structure of ZnO@C NPs were characterized by Fourier transform infrared spectroscopy (FTIR) and X-ray photoelectron

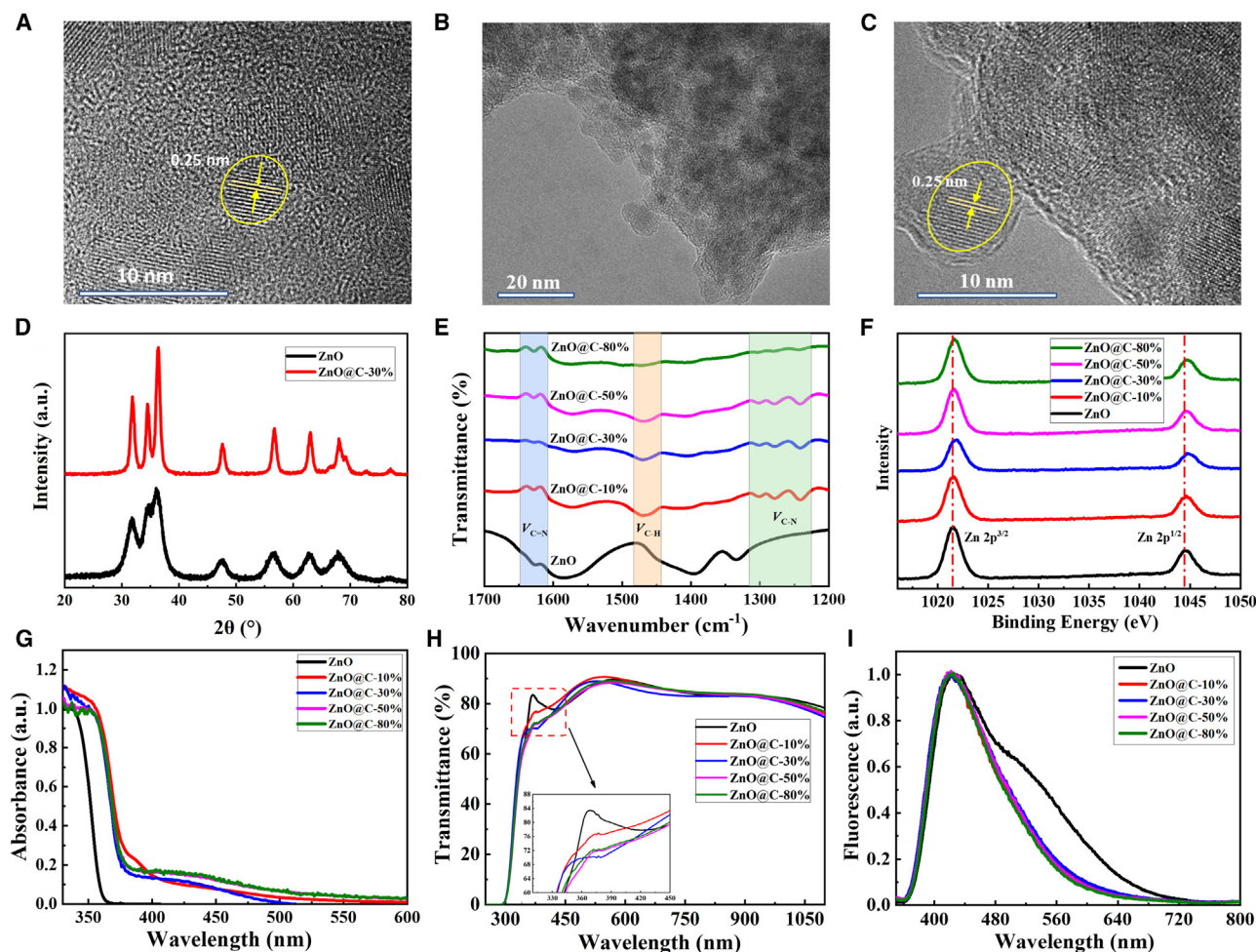


Figure 2. Morphology, structure, and optical properties of ZnO@C NPs

- (A) Partially magnified HR-TEM image of ZnO NPs.
 (B and C) Partially magnified HR-TEM image of ZnO@C NPs-30%.
 (D) XRD pattern of ZnO (black) and ZnO@C-30% (red) films.
 (E) Partially magnified FTIR spectra of ZnO and ZnO@C NPs.
 (F) Zn 2p^{3/2} and Zn 2p^{1/2} XPS spectra of ZnO and ZnO@C NPs.
 (G) UV-vis spectra of ZnO and ZnO@C films.
 (H) Transmittance spectra (inset: local enlarged illustration of transmittance spectra) of ZnO and ZnO@C films.
 (I) PL spectra (excitation at 350 nm) of ZnO and ZnO@C films.

spectroscopy (XPS). Figure S2 shows the FTIR spectra of different samples, where Zn–O vibrational bands are observed at 420–600 cm⁻¹ in both ZnO and ZnO@C NPs.^{32,33} The bands located at 650 and 1,470 cm⁻¹ of ZnO@C NPs are attributed to Zn–N and the C=C vibrational bands of the benzene ring within the carbon layer,^{33,34} respectively. The –OH vibrational band located at 3,200–3,500 cm⁻¹ was observed in ZnO NPs, while the appearance of a double band is observed in ZnO@C NPs at 3,200–3,400 cm⁻¹, which belongs to the N–H vibrational band.³⁵ Further magnified analysis of FTIR spectra in the range of 1,200–1,700 cm⁻¹ is shown in Figure 2E, and there is a vibrational band at 1,629 cm⁻¹ for C=N bonds and at 1,224–1,313 cm⁻¹ in ZnO@C NPs.³⁵ Combined with the C=C vibrational band attributed to the benzene ring at 1,470 cm⁻¹, it is assumed that ZnO@C NPs contain a phenazine structure, while none of these vibrational bands in ZnO NPs were

observed. The above results suggest that *o*-phenylenediamine reacts with ZnO NPs, bonds together, and further self-polymerizes.

In the full XPS spectrum of ZnO@C NPs (Figure S3), the peak attributed to the N 1s is observed at 400 eV,²⁶ while the peak was not observed in ZnO NPs, corroborating the presence of carbon shells on the surface of ZnO NPs, as indicated by the TEM and FTIR results. The XPS spectra of Zn element in ZnO and ZnO@C NPs are further analyzed by split peak fitting (Figure 2F). The binding energy bands of element Zn (Zn 2p^{3/2} and Zn 2p^{1/2}) show a tendency to shift toward the high-energy direction, indicating that ZnO NPs are bonded to the *o*-phenylenediamine through reaction.³⁶ What's important is that the variation of defect states in ZnO can be observed more clearly for O elemental bands. For ZnO, the bands of oxygen element at 530 and 531 eV can be attributed to lattice oxygen and defective oxygen, respectively. The larger the ratio of lattice oxygen to defective oxygen, the fewer are the ZnO defects.^{37,38} The O 1s splitting results of ZnO and ZnO@C NPs are shown in Figure S4, where C1 and C2 represent the lattice oxygen and defective oxygen, respectively. As seen in Figure S4, the percentage of lattice oxygen of ZnO NPs is 43.72%, while the percentages of lattice oxygen of ZnO@C-10%, ZnO@C-30%, ZnO@C-50%, and ZnO@C-80% NPs are 45.85%, 59.03%, 61.51%, and 70.61%, respectively. Obviously, the oxygen defects of ZnO@C NPs are significantly suppressed by the surface carbon shell.

In order to further reveal the formation process of ZnO@C NPs, the ¹H nuclear magnetic resonance spectra of ZnO NPs, *o*-phenylenediamine, and ZnO@C NPs were compared, as shown in Figure S5. As the synthesized ZnO@C NPs are uniformly dispersed in methanol, methanol-*d*₄ was chosen as the test solvent. Although the solvent peak of methanol-*d*₄ inevitably obscures the signal of hydroxyl hydrogen in ZnO, fortunately, the existence of hydrogen bond can be concluded based on the shift of amino hydrogen from 4.14 to 4.21 ppm before and after the reaction. In addition, the presence of the coordinate covalent bond can be inferred from the observation that the number of amino hydrogens is only one-third of the initial count before the reaction, when the number of aromatic hydrogens in *o*-phenylenediamine and ZnO@C NPs are kept constant.³⁹ In a word, it can be concluded that both hydrogen bonds and coordinate covalent bonds exist between *o*-phenylenediamine and ZnO NPs.

Based on the above morphological and structural characterization results, it is speculated that the formation mechanism of the ZnO@C NPs is as follows (Figure 1). First of all, when ZnO NPs and *o*-phenylenediamine are evenly mixed in methanol, the hydroxyl group on the surface of ZnO NPs and the amino group of *o*-phenylenediamine form hydrogen bonds, and the amino group and Zn form coordination bonds. The two kinds of bonds combine to form a layer of *o*-phenylenediamine molecular layer coated on the ZnO NPs. Furthermore, the outer *o*-phenylenediamine molecular layer of ZnO NPs is self-polymerized and further carbonized to form a dense carbon layer under high temperature and pressure. Eventually, a core-shell structure of carbon-coated ZnO NP, that is, ZnO@C NP, is generated.⁴⁰

Optical properties of ZnO@C NPs

Considering that the optical properties of the ETL have a crucial impact on the performance of OSCs, the ultraviolet and visible (UV-vis) spectrophotometry, photoluminescence (PL) and transmittance characterizations of ZnO@C NPs were carried out. Compared to ZnO NPs, the absorption edges of the intrinsic absorption peak attributed to ZnO in ZnO@C NPs show obvious red shift (Figure 2G),

probably due to the increased ZnO grain size, which is confirmed by the XRD results (Figure 2D). In addition, the absorption of ZnO@C NPs is significantly stronger than that of ZnO NPs in the UV region, mainly because of the strong UV absorption characteristics of their surface carbon shell. A new absorption band at 400–480 nm is also tested for ZnO@C NPs, which is ascribed to the absorption band of the carbon shell on the ZnO NPs' surface. However, the additional absorption band in the visible region of ZnO@C NPs brings another effect, which might reduce the absorption of photons by the active layer materials in OSCs. Thus, the optical transmittance of ZnO and ZnO@C ETLs with the same thickness was further characterized, as seen in Figure 2H. The optical transmittance values of ZnO film and ZnO@C-10%, ZnO@C-30%, ZnO@C-50%, and ZnO@C-80% films are calculated to be 80.53%, 81.20%, 79.47%, 79.43%, and 80.17%, respectively, according to the integration of the transmittance curves. Obviously, the carbon shells coated on the ZnO NPs have little effect on the light transmission performance of the ZnO@C ETL films, so the coating does not significantly affect the device light absorption.

As shown in Figure 2I, both ZnO and ZnO@C films have strong ZnO intrinsic PL emission spectra at 420 nm. In addition, a broad emission band at 480–600 nm is detected for ZnO film, which is a PL band due to oxygen vacancy defects in ZnO,^{22,41} while none of these bands are found in ZnO@C films. This indicates that the carbon shell effectively passivates the oxygen vacancy defects in ZnO NPs, which not only can facilitate the charge transfer but also can inhibit the catalytic reaction triggered by defective state.^{17,18}

Good solvent dispersion and long-term stability are essential for ZnO@C NPs to be used in OSCs, and the zeta potential value can clearly reflect these properties. Specifically, the positive and negative zeta potential values are opposite of the charge of the charged particles, and their absolute values reflect the stability of the nanoparticles.⁴² In this regard, the zeta potentials of ZnO and ZnO@C NPs were tested. As shown in Figure S6, the results show that the zeta potentials of all ZnO@C NPs samples are larger than that of pristine ZnO NPs (24.7 mV), and the maximum potential value of 30.4 mV is reached for ZnO@C-30% NPs. ZnO@C NPs exhibit better dispersion and long-term stability than ZnO NPs, which is mainly because the abundant functional groups on the surface of the carbon shell enhance their affinity with solvents.

Photovoltaic performance of ZnO@C NP-based OSCs

To investigate the feasibility of ZnO@C NPs as ETL materials for OSCs, inverted OSCs with the structure of ITO/ETL/PM6:Y6(PM6:L8-BO)/MoO₃/Al were fabricated and characterized. The chemical structure of active materials, current density-voltage (*J*-*V*) curves, and external quantum efficiency (EQE) spectra of OSCs are displayed in Figure 3, and the device parameters of OSCs are listed in Table 1. For the PM6:Y6 OSCs, the optimal device based on ZnO NPs yields a PCE of 15.79%, with short circuit current density (*J*_{SC}) of 26.46 mA cm⁻², open circuit voltage (*V*_{OC}) of 0.838 V, and fill factor (FF) of 0.7122, comparable to the level previously reported in the literature.⁴³ The ZnO@C-30% NP-based PM6:Y6 devices achieve a champion PCE of 16.25%, with *J*_{SC} of 26.25 mA cm⁻², *V*_{OC} of 0.842 V, and FF of 0.7354. For the PM6:L8-BO OSCs, devices based on different ETLs show the same trend. ZnO@C-30% NP-based OSCs show higher PCE of 17.55% than that of ZnO NP-based OSCs (16.92%). The ZnO@C NP-based devices obtain a higher PCE compared to ZnO NP-based devices thanks to their higher *V*_{OC} and FF.

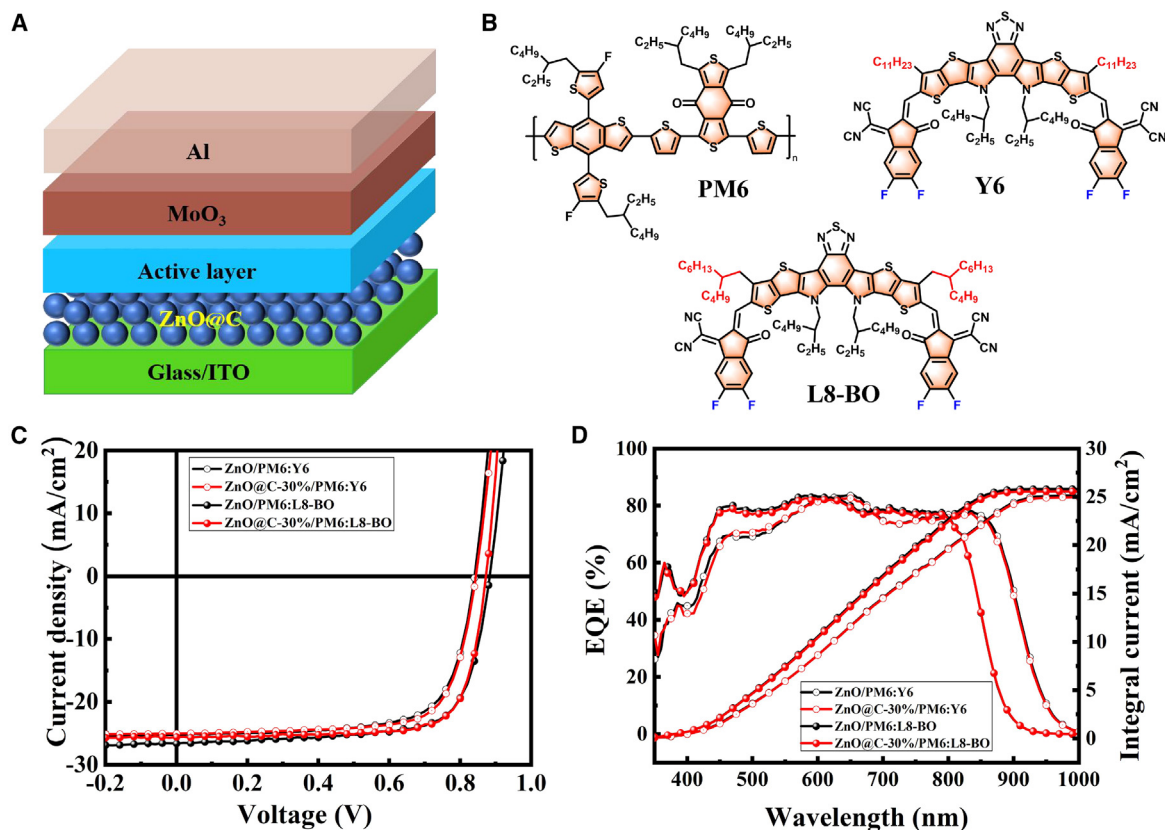


Figure 3. Photovoltaic performance of ZnO@C NP-based OSCs

- (A) Structure diagram of OSCs devices.
 (B) Chemical structure of PM6, Y6, and L8BO.
 (C) J-V curves of OSCs based on different ETLs.
 (D) EQE spectra of OSCs based on different ETLs.

OSCs based on ZnO@C NPs have a higher V_{OC} than devices based on ZnO NPs, which may be due to a modification of the work function (W_F) of ZnO@C NPs to achieve an energy level that better matches that of the active layer. To verify the conjecture, the W_F values of ZnO@C thin films were characterized by ultraviolet photoelectron spectroscopy (UPS). As shown in Figure 4A, the W_F (3.60–3.89 eV) of ZnO@C films is significantly reduced compared to that of ZnO films (4.04 eV), which can enhance the built-in electric field in OSCs and inhibit the charge recombination between active layer and cathode, ultimately achieving higher V_{OC} .⁴⁴ Meanwhile, the W_F values of ZnO, ZnO@poly(phthalimide), and ZnO@C were also calculated by density functional theory (DFT) (Figures 4B, 4C, and S8). The constructed heterojunction model and density of states of ZnO, ZnO@poly(phthalimide), and ZnO NPs are shown in Figures S7 and S9. The W_F calculated from the theoretical simulations is in general agreement with the results of the actual tests, with the standard ZnO at 4.34 eV and reduced to 3.828 eV and 3.934 eV after coating with poly(phthalimide) and carbon layer, respectively.

Furthermore, the diode characteristics of ZnO@C NP-based OSCs were tested in dark condition. As shown in Figure 4D, the reverse saturation currents of devices with a ZnO@C ETL are significantly suppressed, while all devices exhibit similar output currents in the forward direction compared to devices with a pristine ZnO ETL, indicating the superior charge selectivity and charge transfer capability of the

Table 1. Device parameters of PM6:Y6 or PM6:L8-BO OSCs based on different ETLs

Active layer	ETL	V_{OC} (V)	J_{SC} (mA/cm ²)	FF (%)	PCE (%)
PM6:Y6	ZnO	0.838	26.46	71.22	15.79
	ZnO@C-10%	0.843	25.89	72.30	15.78
	ZnO@C-30%	0.842	26.25	73.54	16.25
	ZnO@C-50%	0.842	26.23	72.46	16.00
PM6:L8-BO	ZnO	0.881	26.51	72.44	16.92
	ZnO@C-30%	0.883	25.95	76.59	17.55

ZnO@C NP-based devices.⁴⁵ Further, the diode parameters of the device are fitted according to equation⁴⁶ $J = J_0 \left\{ \exp \left[\frac{q(V - J R_{sh})}{nk_B T} \right] - 1 \right\} + \frac{V - J R_s}{R_{sh}} - J_{ph}$. Where, J_0 , q , n , R_s , R_{sh} , k_B , T , and J_{ph} represent the reverse saturation current density, meta-charge, ideal factor of the diode, series resistance, parallel resistance, Boltzmann's constant, thermodynamic temperature, and photogenerated current density, respectively. The resulting fitted parameters are summarized in Table S1. The results show that the ZnO@C NP-based devices show lower J_0 , n and larger R_{sh} and R_s , compared to ZnO NP-based devices. The lower J_0 means stronger charge extraction capability for the ZnO@C ETL. The n values (<1.98) of ZnO@C-10%, ZnO@C-30%, and ZnO@C-50% NP-based devices are lower than those of ZnO NP-based devices (2.03), which indicates a lower charge recombination at the ZnO@C ETL interface. ZnO@C-10%, ZnO@C-30%, and ZnO@C-50% NP-based devices show higher R_{sh} , which implies that the carbon shell on the surface of ZnO@C NPs significantly suppresses the defects of ZnO NPs,^{47,48} resulting in a lower charge recombination rate. The ZnO@C NP-based device shows higher R_s , probably because the carbon shell on the surface reduces the electrical conductivity, which can be proved by the subsequent characterization results of the space charge limited current (Figure 4F).

The transient photovoltage (TPV) test was used to further assess the charge recombination at the ETL/active layer interface. The results are shown in Figure 4E, where the photovoltage decay time in the ZnO@C-30% NP-based OSCs is 35.44 μ s, larger than that in the ZnO NP device (24.53 μ s), which further confirms that the carbon shell suppresses the carrier recombination induced by the defect state. It also can be inferred from the charge extraction kinetics that there is a high electronic coupling between the ZnO@C films and active layer, which may be due to the formation of a tight interface between the ZnO@C films and active layer.

To reveal the J_{SC} drop in ZnO@C NP-based devices, the electron mobility of the ZnO and ZnO@C ETLs was characterized. Single-electron devices with the structure of ITO/ZnO (ZnO@C-30%)/Al were tested (Figure 4F). The electron mobility is calculated by the Mott-Gurney equation: $J = \frac{2}{8} \epsilon \epsilon_0 \mu \frac{V^2}{L^3}$. Where, L represents the ZnO layer thickness, ϵ_0 represents the dielectric constant in free space, which is 8.85×10^{-12} F/m, ϵ is the relative dielectric constant of the material, which is 8.66 for ZnO,⁴⁹ V is the applied bias voltage, and J is the corresponding current. The calculated electron mobilities for ZnO and ZnO@C-30% films are 1.93×10^{-3} cm²V⁻¹S⁻¹ and 1.04×10^{-3} cm²V⁻¹S⁻¹, respectively. The electron mobility of ZnO@C-30% ETLs decreases compared to ZnO ETLs, which is the main reason for the slight decrease in the device J_{SC} . From the results of the theoretical simulations (Figure S8), the total density of states values at the Fermi energy level are also reduced. The results support the view that the cladding structure affects the electron mobility of ZnO, that the cladding may be incomplete, and that further improvements in the cladding are needed and would be a more promising material.

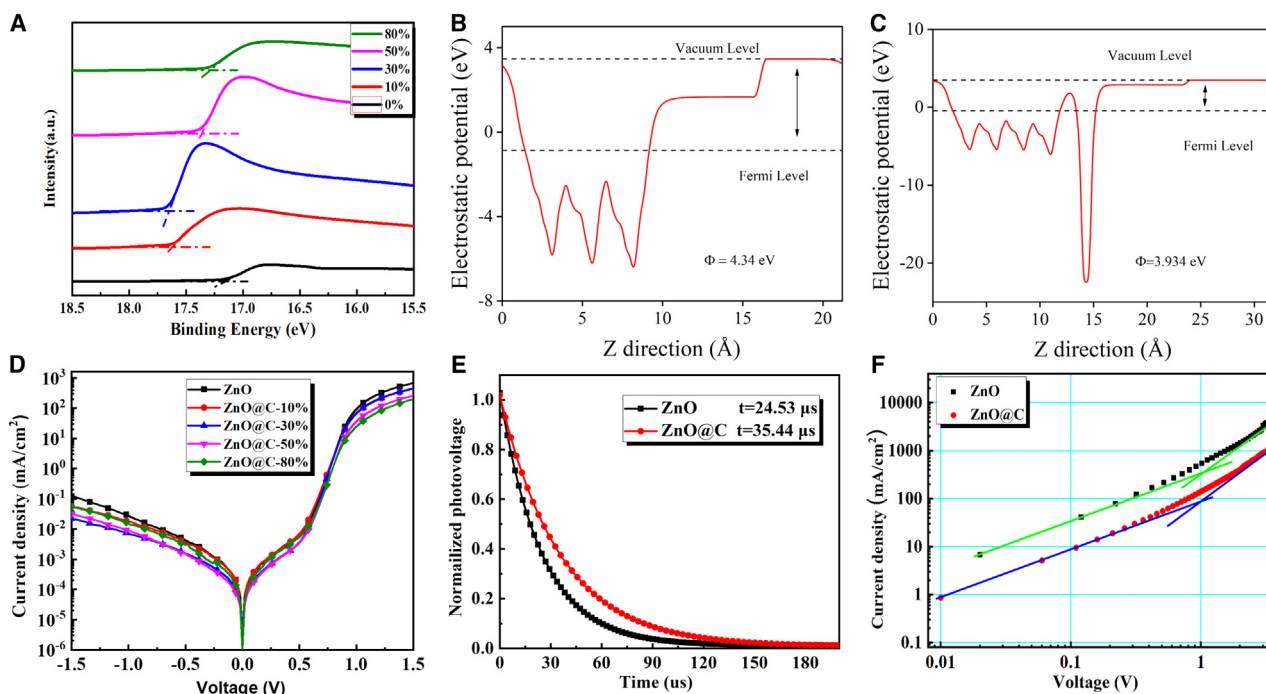


Figure 4. Optoelectronic properties of ZnO@C ETLs

- (A) UPS spectra of the ZnO and ZnO@C films.
 (B) Work functions calculated by DFT for ZnO.
 (C) Work functions calculated by DFT for ZnO@C.
 (D) Dark J-V curves of PM6:Y6 devices based on different ETLs.
 (E) Normalized TPV curves of ZnO and ZnO@C-30%-based OSCs under 100 mW cm^{-2} .
 (F) J-V characterization of the electron-only devices with a structure of ITO/ZnO (ZnO@C-30%)/Al.

The surface morphology of the ZnO and ZnO@C films was examined by atomic force microscopy (AFM) characterization (as shown in Figure S10). The surface roughness (root mean square, R_{rms}) of ZnO films is 3.08 nm, while the R_{rms} values of ZnO@C-10%, ZnO@C-30%, ZnO@C-50%, and ZnO@C-80% films are 7.15, 7.16, 6.03, and 6.01 nm, respectively. The greater surface roughness facilitates the formation of more contact points, resulting in better contact at the ZnO@C/active layer interface, improving the FF and the long-term stability of the device.

In conclusion, ZnO@C NPs have better matching energy levels and better ohmic contacts with the active layer. Furthermore, the ZnO@C NPs show fewer surface defect states, lowering the electron transport potential barrier and suppressing exciton recombination in the ZnO/active layer. Ultimately, ZnO@C NPs as an ETL can simultaneously improve the V_{OC} and FF of the devices.

Stability of ZnO@C NP-based OSCs

The permanent stability of OSCs is a key requirement for their commercialization, especially for the air stability and UV stability. Firstly, the air stability values of ZnO ETL-based OSCs at different humidity levels (0%, 30%, 60%, and 100%) were compared. The V_{OC} of OSCs is most sensitive when decaying in air, so we investigated the V_{OC} aging of OSCs at different humidities, as shown in Figure S11. Obviously, the V_{OC} decay rate of the ZnO ETL-based OSCs is positively correlated with the air humidity, and the higher the humidity, the faster is the decay rate of V_{OC} . This demonstrates that ZnO NPs are very sensitive to moisture in the air, resulting

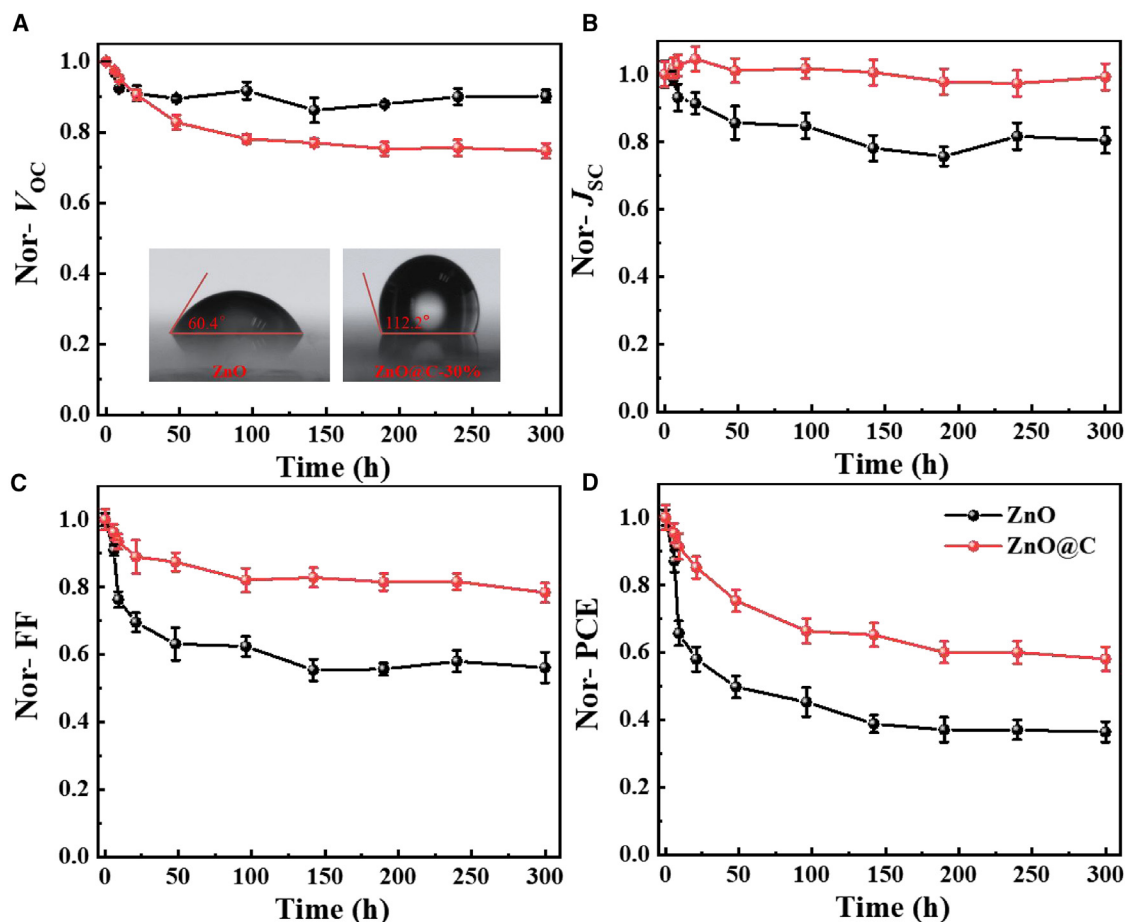


Figure 5. Air stability of ZnO@C NP-based OSCs

(A–D) Normalization decay of V_{OC} (A), J_{SC} (B), FF (C), and PCE (D) in 60% humidity for PM6:Y6-based inverted OSCs using ZnO and ZnO@C-30% NPs as the ETL (insets: images of water contact angle for ZnO and ZnO@C-30% films). The error bar indicates standard deviation.

in poor air stability of OSCs. Then, the air stability of ZnO NP- and ZnO@C-30% NP-based devices under high humidity (60%) was investigated. As seen in Figure 5, after aging in the air for 300 h, the PCE of a ZnO NP-based device decreased by 63%, along with a decrease in V_{OC} by 10%, J_{SC} by 20%, and FF by 44%. However, the ZnO@C-30% NP-based devices show significantly improved air stability. After aging in the air, the PCE of the ZnO@C-30% NP-based device decreased by 42%, significantly less than that of ZnO NP-based devices, which was mainly due to the more stable J_{SC} (decreased by 1%) and FF (decreased by 22%). It is speculated that the improvement of air stability of the ZnO@C NP-based device mainly is due to the carbon shell coated on the surface of the ZnO NPs inhibiting the damage of ZnO by water and oxygen in the air.

To verify the above speculation, the water and diiodomethane contact angles of ZnO and ZnO@C films were characterized (Figure S12), the relevant contact angle data are summarized in Table S2. From the results, the water contact angle of ZnO films is 60.4°, while the contact angle of ZnO@C films increases significantly and reaches the maximum (112.2°) when the precursor *o*-phenylenediamine content is 30%. The larger water contact angles of ZnO@C films indicate that the carbon shell coated on ZnO NPs has high hydrophobicity, thanks to its rich amine functional groups, which

has been confirmed by the results of FTIR and XPS results. ZnO has been reported to experience chemical dissolution when exposed to water,^{50,51} which can be accelerated under illumination. Therefore, the high hydrophobicity of ZnO@C NPs is conducive to the isolation of water in the air and ensures the long-term air stability of the ZnO@C NP-based OSCs. In addition, the opposite situation was observed in the contact angle test of diiodomethane (Figure S12B), where the contact angles of diiodomethane for ZnO@C films (15.1°–34.3°) are smaller than that of ZnO films (50.1°), indicating that the ZnO@C NPs have better compatibility with the active layer, which facilitated the film formation of active layer molecules on its surface. The good contact interface between the ZnO@C/active layers facilitates the reduction of interfacial barriers and promotes charge separation and transfer at the interface, while also improving device stability.

OSCs serving as power source for spacecraft in outer space is another promising application area. However, in outer space, OSCs will be exposed to a lot of UV radiation. The UV stability of OSCs is therefore of great importance for their future application. In this study, the UV stability of ZnO@C-30% NP-based OSC-based devices was further explored in comparison to a ZnO NP-based device. The unencapsulated OSCs were continuously irradiated with a strong UV light source in a glove box filled with N₂, and the device performance was tested after different irradiation times, as shown in Figure 6. After 3 h of strong UV light irradiation, the PCE of ZnO-based OSCs decreases by 69%, along with V_{OC} decreasing by 14%, J_{SC} decreasing by 31%, and FF decreasing by 47%. In contrast, ZnO@C NP-based devices exhibit much higher UV stability than ZnO-based devices. The PCE of ZnO@C NP-based devices decays by 26% after continuous UV light irradiation, which is 2.7 times slower than that of ZnO NP-based devices. All performance parameters of ZnO@C NP-based OSCs show better UV stability than ZnO NP-based devices, especially for J_{SC} and FF.

ZnO is reported to be prone to catalyze the photodecomposition of NFA molecules, which is mainly related to its surface defects.^{52,53} The surface defects can enhance the absorption of ZnO and promote the generation of excitons. The holes can oxidize the dangling OH⁻ to produce hydroxyl radicals, which break the double bond at the linker of the A-D-A structure of NFA, ultimately greatly reducing the efficiency of OSCs. Therefore, the suppression of surface defects in ZnO is a major effective measure to improve the photostability of ZnO-based OSCs. The results of the electron spin resonance (ESR) characterization of ZnO NPs and ZnO@C-30% NPs defect states validate the speculation of an enhanced mechanism for UV stability of ZnO@C-30% NP-based devices. As shown in Figure 7A, a strong surface oxygen vacancy (Vo⁺) and interstitial ZnO (Zn_i⁺) vibrational peak are observed at g = 1.96 for synthetic ZnO NPs.⁵³ While in ZnO@C-30% NPs, the vibrational peak of g = 1.96 is significantly reduced, which indicates that surface defects in the ZnO NPs are effectively passivated by the carbon shell coating. This can block the adsorption of oxygen on the surface of ZnO and ultimately improve the UV stability of the device by inhibiting its photocatalytic reaction.

The UV stability effects of ZnO@C NPs as an ETL in different NFA systems were further compared in Figures 7B, S13, and S14. The standard ZnO/Y6 film shows a significant decrease in the Y6 absorption peak at 820 nm after strong UV irradiation (Figures 7B and S13A), while the ZnO@C-30%/Y6 film is almost unchanged (Figures 7B and S13B), indicating that the carbon layer can effectively protect NFA as a UV absorber. Similarly, we confirmed the same protective effect on IT-4F (Figures S13C, S13D, and S14), which illustrates the generality of ZnO@C NP-based devices for improving the UV stability of non-fullerene-based OSCs.

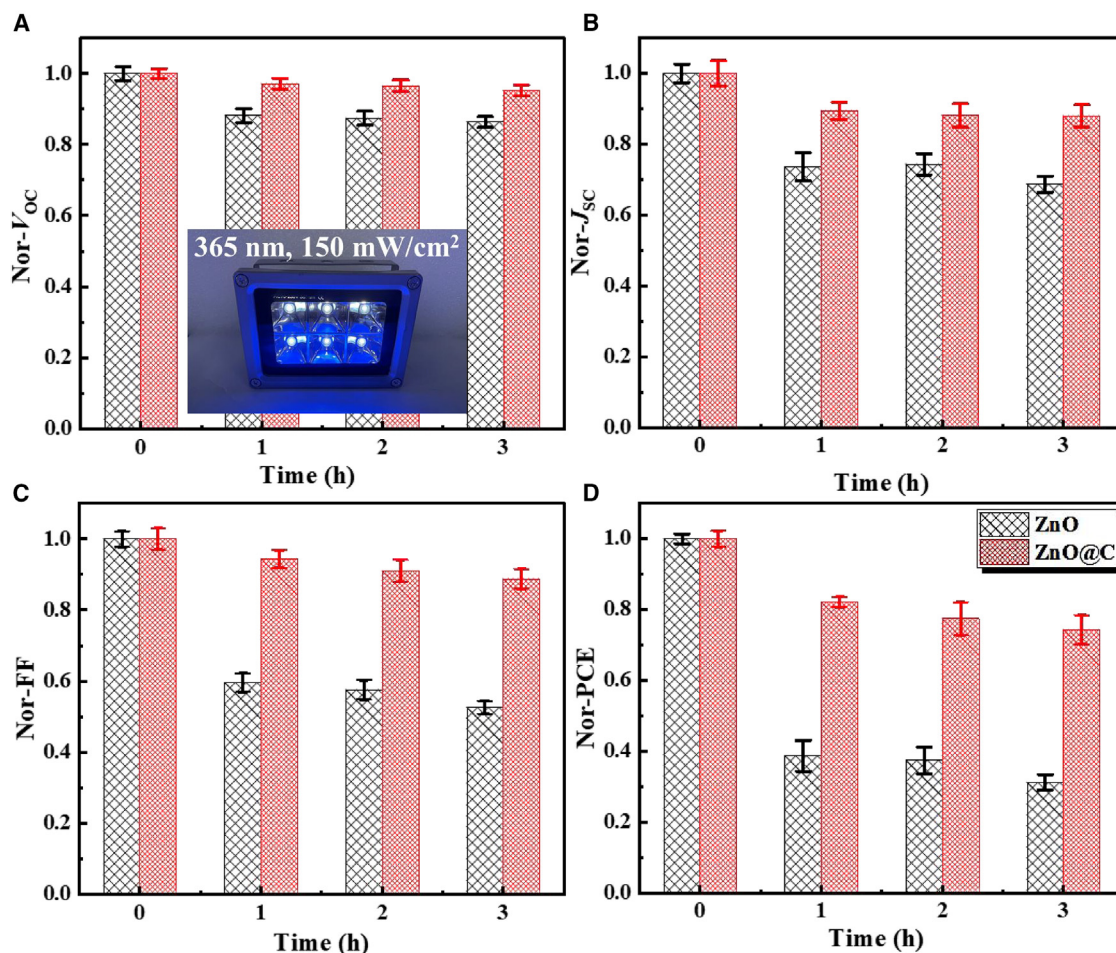


Figure 6. UV stability of ZnO@C NP-based OSCs

(A–D) Normalized decay of V_{oc} (A), J_{sc} (B), FF (C), and PCE (D) of PM6:Y6-based inverted OSCs using ZnO and ZnO@C NPs-30% as ETLs under different UV illumination time (insets: photograph of the UV lamp source used in this experiment). The error bar indicates standard deviation.

Furthermore, to obtain more clarity on the UV stability improvement mechanism of ZnO@C NPs, the products of ZnO/Y6 and ZnO@C/Y6 films after UV illumination for 5 h were characterized by mass spectrometry (MS) measurements (Figure 7C). Pristine Y6 shows a strong peak at m/z value of 1,450.5. As for photo-degraded ZnO/Y6 film, there are several peaks around 200–400 and a peak at 1,237.5. Obviously, the continuous strong UV irradiation accelerates the decomposition of Y6 catalyzed by ZnO NPs,⁵⁴ forming at least four fragments (Figure 7D). However, for the photo-degraded ZnO@C/Y6 film, the peak of 1,237.5 is not detected, while the peaks in the range of 200–400 are much weaker. The above results fully prove that the carbon shell-coated ZnO NPs effectively inhibit the catalytic ability on Y6.

The UV stability of ZnO@C NP-based OSCs shows a significant enhancement effect, but it is not yet fully suppressed, which could be attributed to the following reasons. On the one hand, the quality and uniformity of carbon shell affects its barrier effect on the ZnO NPs and active layer materials, as can be seen in Figure 7C. On the other hand, UV-induced destruction of the active layer is also another factor contributing to the UV-induced aging of OSCs. To further achieve higher UV stability of OSCs, the

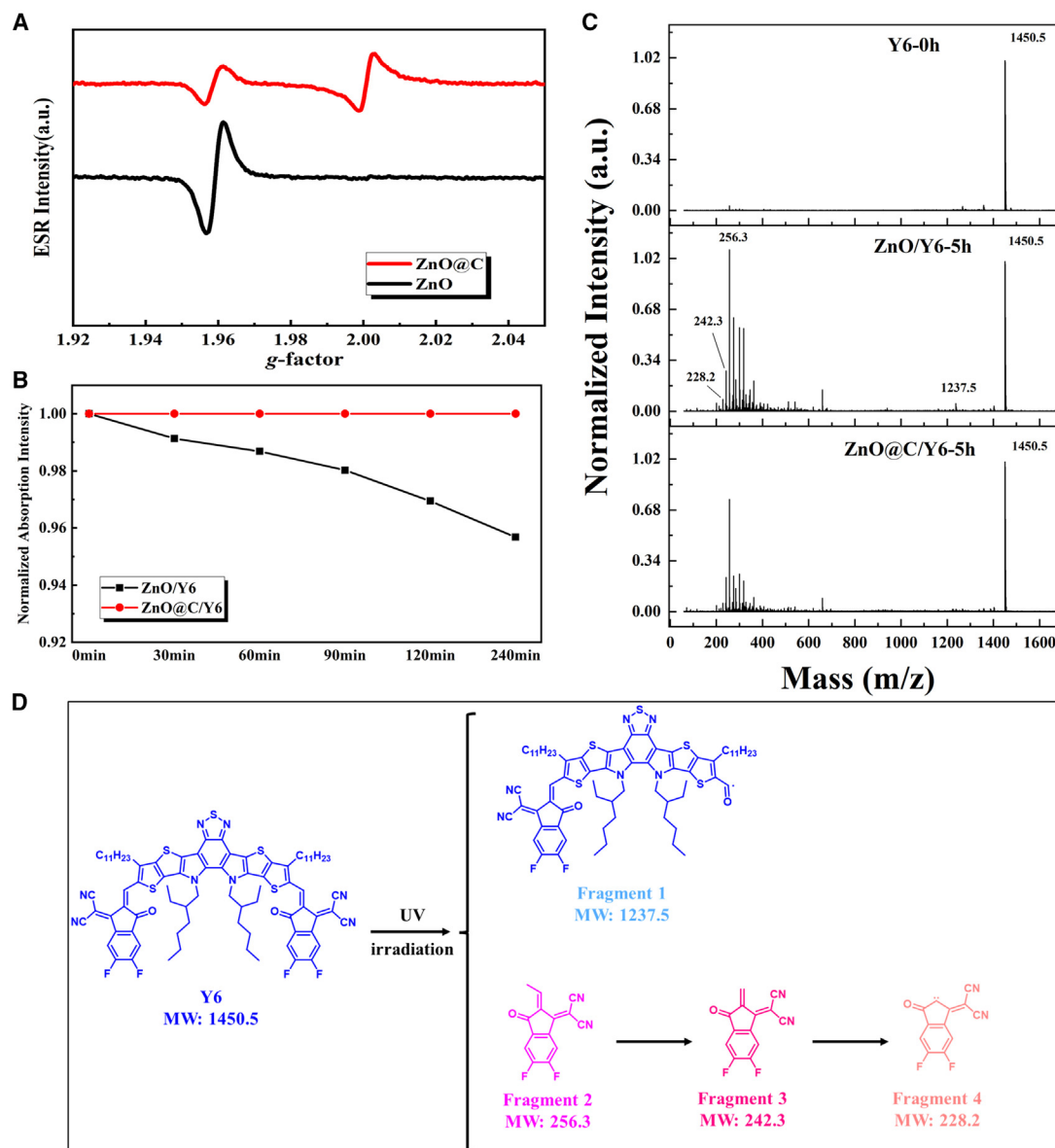


Figure 7. Photochemical characterization of the ZnO@C

(A) ESR spectra of ZnO and ZnO@C-30% films after UV illumination for 5 h.

(B) Variation of the highest absorbance intensity of ZnO/Y6 and ZnO@C-30%/Y6 after strong UV irradiation for different times.

(C) MALDI-MS spectra of the pristine and aged Y6 on ZnO and ZnO@C-30% surfaces after UV illumination for 5 h.

(D) Chemical structure of the decomposed product.

following improvement measures can be considered. (1) Improve the densities of the carbon shell on ZnO NP surfaces by optimization of the synthesis process. (2) Select molecules with strong UV absorption to encapsulate the ZnO NPs. (3) Develop more UV-stable active layer materials.

In conclusion, the ZnO@C NPs with core-shell structure were synthesized and applied as ETLs of OSCs. The ZnO@C NPs exhibit fewer surface defects, better monodispersity, and more suitable W_F (3.89 eV), which created a better ohmic contact with the active layer, suppressed exciton recombination at the interface, and

finally improved the PCE of PM6:L8-BO OSCs from 16.92% to 17.55%. What's important, the ZnO@C NP-based OSCs show better UV and air stability. The surface of ZnO@C NPs is rich in hydrophobic functional groups, which can inhibit the adsorption of water and oxygen in the air, thereby improving the air stability of OSCs. With excellent UV absorption capacity and inertness, the carbon shell on the ZnO@C NP's surface absorbs most of the UV light and passivates the surface defects of ZnO NPs, inhibiting the formation of hydroxyl radicals of ZnO NPs, while preventing direct contact between ZnO and NFA, which protects the NFA from being catalyzed by ZnO, and therefore the ZnO@C NP-based OSCs are more stable under UV illumination. Therefore, ZnO@C NPs are promising ETL materials for efficient, air-stable, and photo-stable OSCs, facilitating the future application of OSCs in architectural integration and outer space.

EXPERIMENTAL PROCEDURES

Resource availability

Lead contact

Further information and requests for resources and materials should be directed to and will be fulfilled by the lead contact, Lingpeng Yan (yanlingpeng@tyut.edu.cn).

Materials availability

The materials in this study will be made available upon request.

Data and code availability

All of the data supporting the results are presented in the main text and supplemental information. Further information and requests for additional data should be directed to the lead contact.

Materials

Zinc acetate dehydrate, *o*-phenylenediamine, and chloroform were purchased from Alfa Aesar. Methanol and KOH were purchased from Sinopharm Chemical Reagent Co. PM6, Y6, IT-4F, and L8-BO were bought from Solarmer Materials, Beijing.

Synthesis of ZnO@C NPs

Firstly, ZnO NPs were synthesized by particle precipitation method. Then, *o*-phenylenediamine and ZnO NPs were miscible in methanol with different proportions (*o*-phenylenediamine: ZnO = 0%, 10%, 30%, 50%, and 80%, [w/w]). The mixture was sealed in an autoclave and heated to 180°C for 10 h. At the end of the reaction, we waited for the autoclave to cool down to room temperature and took out the precipitated samples. It is clear to see that as the content of *o*-phenylenediamine increases, the color of the products gradually changes from light yellow to dark brown. However, the pure ZnO NPs solution did not precipitate or change color even after a high-temperature reaction of 180°C for 10 h. Finally, the product was washed three times by centrifugation using methanol to obtain ZnO@C NPs.

Fabrication of OSCs

The structure of fabricated OSCs devices is ITO/ZnO(ZnO@C)/PM6:Y6/MoO₃/Al. After being ultrasonically cleaned with glass cleaners and 2-propanol, the ITO (indium tin oxide) glasses were exposed to ultraviolet ozone for 30 min. Then, the ETL layer (ZnO or ZnO@C NPs) was spin-coated (2,000 rpm, 60 s) onto the ITO substrate and underwent an annealing process (130°C, 10 min). After that, a solution of active layer (PM6:Y6 = 1:1.2 [w/w], 15.4 mg/mL in chloroform, containing 0.5 vol % chloronaphthalene; PM6:L8BO = 1:1.2 [w/w], 16.5 mg/mL in chloroform, containing 0.25 vol % 1,8-diiodooctane) was spin-coated onto the ETL and underwent an annealing

process (100°C, 10 min). Finally, the MoO₃ and Al electrodes were deposited on the active layer by thermal evaporation.

Characterization of ZnO and ZnO@C NPs

The microscopic and surface morphology of synthesized nanoparticle samples was characterized by AFM and TEM with a JEM-ARM300F, JEOL transmission electron microscope and a Dimension 3100 atomic force microscope, respectively. The surface structure of nanoparticle samples was measured by XPS (UPS) and FTIR using a PHI 5000 Versa III X-ray photoelectron spectroscope and a BRUKER TENSOR 27 spectrometer. XRD spectra of nanoparticle samples were detected by a Rigaku D/max-2500 diffractometer. The light absorption properties of nanoparticle samples were characterized by UV-vis using a Lamada 750 UV/vis/NIR. The photoluminescent properties of nanoparticle samples were tested by PL using a Horiba Fluoromax-4 spectrometers. The ζ potentials of nanoparticle samples were measured by dynamic light scattering using a Malvern granulometer. The ESR spectra of nanoparticle samples were detected in a JEOL JES-X320 spectrometer. The MS spectra of ZnO(ZnO@C)/NFA before and after continuous illumination of UV light were tested with an ultrafleXtreme MALDI-TOF/TOF mass spectrometer.

Theoretical calculation

Under the generalized gradient approximation condition, we use the Perdew-Burke-Ernzerhof⁵⁵ formulation for all DFT calculations under first principles.^{56,57} The projected augmented wave potentials^{58,59} have been chosen to describe the ionic cores, and the valence electrons have been taken into account by using a plane wave basis set with a kinetic energy cutoff of 450 eV. We used a Gaussian smearing method to allow for partial occupancy of the Kohn-Sham orbitals where a width of 0.05 eV was used. Further, integration of the Brillouin zone was performed using 0.04 *k*-mesh Monkhorst-Pack sampling⁶⁰ to optimize geometry and lattice size. The convergence energy threshold for the self-consistent calculations is 10⁻⁵ eV. We have optimized the equilibrium geometry and lattice constants under the condition that the maximum stress on each atom not exceed 0.02 eV Å⁻¹. For the purpose of eliminating artificial interactions between periodic images, we added a vacuum layer of 17 Å to the surface. Based on the empirical correction in Grimme's scheme, the weak interactions are described by the DFT+D3 method.^{61,62}

Characterization of OSCs

The performance parameters of unencapsulated OSCs were tested in a N₂-filled glove box using a Sirius SS150A sun simulator (100 mW/cm², Zolix), and the experimental data were recorded by a Keithley 2400 source meter. The EQE system consists of a probe light (150 W tungsten halogen lamp, Osram 64610), a monochromator (Zolix, Omni-k300), an I-V converter (D&R-IV Converter, Suzhou D&R Instruments), and a lock-in amplifier (Stanford Research Systems SR 830). In addition, a standard silicon cell was used as a reference to correct device performance. For UV stability testing, the unencapsulated OSCs were continuously irradiated with a UV light source (365 nm, 150 mW/cm²) in a N₂-filled glove box, and the device performance was characterized after different irradiation times.

SUPPLEMENTAL INFORMATION

Supplemental information can be found online at <https://doi.org/10.1016/j.xcrp.2023.101654>.

ACKNOWLEDGMENTS

This work is supported by the National Natural Science Foundation of China (61904121, 22075315), Shanxi-Zheda Institute of Advanced Materials and Chemical Engineering (2022SX-TD012, 2021SX-TD012), and Youth Innovation Promotion Association of CAS (2019317).

AUTHOR CONTRIBUTIONS

L.P.Y., Y.Y.Y., and C.-Q.M. conceived the idea and designed the experiment. W.S.Z., and Y.W. synthesized ZnO@C NPs. Y.L.H. synthesized ZnO NPs. Y.W. and H.T.S. carried out the device fabrication. H.Z. carried out the device characterization. H.T.H. and F.L. conducted the theoretical calculation. Q.M.S. conducted the TEM. L.P.Y. and W.S.Z. prepared the manuscript. Y.Z.Y., C.-Q.M., and H.W. were involved in discussions and helped revise the manuscript. All the authors discussed the results and commented on the manuscript.

DECLARATION OF INTERESTS

The authors declare no competing interests.

Received: July 13, 2023

Revised: September 4, 2023

Accepted: September 29, 2023

Published: October 25, 2023

REFERENCES

- Liu, Y., Kumbalathan, T., Feng, W., Pang, B., Tao, J., Xu, J., Xiao, H., Joyce, M.A., Tyrrell, D.L., Zhang, H., et al. (2022). Recent progress in organic solar cells (Part I material science). *ACS Meas. Sci. Au* 2, 224–232. <https://doi.org/10.1007/s11426-021-1180-6>.
- Fu, J., Fong, P.W.K., Liu, H., Huang, C.S., Lu, X., Lu, S., Abdelsamie, M., Kodalle, T., Sutter-Fella, C.M., Yang, Y., and Li, G. (2023). 19.31% binary organic solar cell and low non-radiative recombination enabled by non-monotonic intermediate state transition. *Nat. Commun.* 14, 1760. <https://doi.org/10.1038/s41467-023-37526-5>.
- Li, Y., Huang, X., Ding, K., Sherif, H.K.M., Jr., Ye, L., Liu, H., Li, C.Z., Ade, H., and Forrest, S.R. (2021). Non-fullerene acceptor organic photovoltaics with intrinsic operational lifetimes over 30 years. *Nat. Commun.* 12, 5419. <https://doi.org/10.1038/s41467-021-25718-w>.
- Du, X., Heumueller, T., Gruber, W., Classen, A., Unruh, T., Li, N., and Brabec, C.J. (2019). Efficient polymer solar cells based on non-fullerene acceptors with potential device lifetime approaching 10 years. *Joule* 3, 215–226. <https://doi.org/10.1016/j.joule.2018.09.001>.
- Park, S., and Son, H.J. (2019). Intrinsic photo-degradation and mechanism of polymer solar cells: the crucial role of non-fullerene acceptors. *J. Mater. Chem. A* 7, 25830–25837. <https://doi.org/10.1039/C9TA07417A>.
- Classen, A., Heumueller, T., Wabra, I., Gerner, J., He, Y., Einsiedler, L., Li, N., Matt, G.J., Osvet, A., Du, X., et al. (2019). Revealing hidden UV instabilities in organic solar cells by correlating device and material stability. *Adv. Energy Mater.* 9, 1902124. <https://doi.org/10.1002/aenm.201902124>.
- Tang, H., Bai, Y., Zhao, H., Qin, X., Hu, Z., Zhou, C., Huang, F., and Cao, Y. (2023). Interface engineering for highly efficient organic solar cells. *Adv. Mater.* 2212236. <https://doi.org/10.1002/adma.202212236>.
- Qin, F., Wang, W., Sun, L., Jiang, X., Hu, L., Xiong, S., Liu, T., Dong, X., Li, J., Jiang, Y., et al. (2020). Robust metal ion-chelated polymer interfacial layer for ultraflexible non-fullerene organic solar cells. *Nat. Commun.* 11, 4508. <https://doi.org/10.1038/s41467-020-18373-0>.
- Ahmad, N., Zhou, H., Fan, P., and Liang, G. (2021). Recent progress in cathode interlayer materials for non-fullerene organic solar cells. *EcoMat* 4, e12156. <https://doi.org/10.1002/eom2.12156>.
- Ahmad, N., Liang, G., Fan, P., and Zhou, H. (2022). Anode interfacial modification for non-fullerene polymer solar cells: Recent advances and prospects. *InfoMat* 4, e12370. <https://doi.org/10.1002/inf2.12370>.
- Chen, Z., Wang, J., Wu, H., Yang, J., Wang, Y., Zhang, J., Bao, Q., Wang, M., Ma, Z., Tress, W., and Tang, Z. (2022). A transparent electrode based on solution-processed ZnO for organic optoelectronic devices. *Nat. Commun.* 13, 4387. <https://doi.org/10.1038/s41467-022-32010-y>.
- Wang, Z., Guo, J., Pan, Y., Fang, J., Gong, C., Mo, L., Luo, Q., Lin, J., and Ma, C. (2023). Manipulating the macroscopic and microscopic morphology of large-area gravure-printed ZnO films for high-performance flexible organic solar cells. *Energy Environ. Mater.* e12592. <https://doi.org/10.1002/eem2.12592>.
- Jiang, Y., Sun, L., Jiang, F., Xie, C., Hu, L., Dong, X., Qin, F., Liu, T., Hu, L., Jiang, X., and Zhou, Y. (2019). Photocatalytic effect of ZnO on the stability of nonfullerene acceptors and its mitigation by SnO₂ for nonfullerene organic solar cells. *Mater. Horiz.* 6, 1438–1443. <https://doi.org/10.1039/c9mh00379g>.
- Li, P., Jiu, T., Tang, G., Wang, G., Li, J., Li, X., and Fang, J. (2014). Solvents induced ZnO nanoparticles aggregation associated with their interfacial effect on organic solar cells. *ACS Appl. Mater. Interfaces* 6, 18172–18179. <https://doi.org/10.1021/am5051789>.
- Guo, J., Han, Y., Xu, Z., Zha, W., Fang, J., Luo, Q., Liu, L., and Ma, C.Q. (2022). Monodispersed ZnO nanoink and ultra-smooth large-area ZnO films for high performance and stable organic solar cells. *Flex. Print. Electron.* 7, 025013. <https://doi.org/10.1088/2058-8585/ac6fa3>.
- Wei, J., Ji, G., Zhang, C., Yan, L., Luo, Q., Wang, C., Chen, Q., Yang, J., Chen, L., and Ma, C.Q. (2018). Silane-capped ZnO nanoparticles for use as the electron transport layer in inverted organic solar cells. *ACS Nano* 12, 5518–5529. <https://doi.org/10.1021/acsnano.8b01178>.
- Günther, M., Lotfi, S., Rivas, S., Blätte, D., Hofmann, J., Bein, T., and Ameri, T. (2023). The neglected influence of zinc oxide light-soaking on stability measurements of inverted organic solar cells. *Adv. Funct. Mater.* 33, 2209768. <https://doi.org/10.1002/adfm.202209768>.
- Chen, S., Small, C.E., Amb, C.M., Subbiah, J., Lai, T.h., Tsang, S.W., Manders, J.R., Reynolds, J.R., and So, F. (2012). Inverted polymer solar

- cells with reduced interface recombination. *Adv. Energy Mater.* 2, 1333–1337. <https://doi.org/10.1002/aenm.201200184>.
19. Fu, P., Guo, X., Zhang, B., Chen, T., Qin, W., Ye, Y., Hou, J., Zhang, J., and Li, C. (2016). Achieving 10.5% efficiency for inverted polymer solar cells by modifying the ZnO cathode interlayer with phenols. *J. Mater. Chem. A* 4, 16824–16829. <https://doi.org/10.1039/C6TA07105H>.
 20. Yang, K., Fu, J., Hu, L., Xiong, Z., Li, M., Wei, X., Xiao, Z., Lu, S., and Sun, K. (2018). Impact of ZnO photoluminescence on organic photovoltaic performance. *ACS Appl. Mater. Interfaces* 10, 39962–39969. <https://doi.org/10.1021/acsami.8b14224>.
 21. Zhu, X., Guo, B., Fang, J., Zhai, T., Wang, Y., Li, G., Zhang, J., Wei, Z., Duhm, S., Guo, X., et al. (2019). Surface modification of ZnO electron transport layers with glycine for efficient inverted non-fullerene polymer solar cells. *Org. Electron.* 70, 25–31. <https://doi.org/10.1016/j.orgel.2019.03.039>.
 22. Bai, S., Jin, Y., Liang, X., Ye, Z., Wu, Z., Sun, B., Ma, Z., Tang, Z., Wang, J., Würfel, U., et al. (2015). Ethanedithiol treatment of solution-processed ZnO thin films: controlling the intragap states of electron transporting interlayers for efficient and stable inverted organic photovoltaics. *Adv. Energy Mater.* 5, 1401606. <https://doi.org/10.1002/aenm.201401606>.
 23. Lan, A., Li, Y., Zhu, H., Zhu, J., Lu, H., Do, H., Lv, Y., Chen, Y., Chen, Z., Chen, F., and Huang, W. (2023). Improved efficiency and stability of organic solar cells by interface modification using atomic layer deposition of ultrathin aluminum oxide. *Energy Environ. Mater.* e12620. <https://doi.org/10.1002/eem2.12620>.
 24. Lin, X., Yang, Y., Nian, L., Su, H., Ou, J., Yuan, Z., Xie, F., Hong, W., Yu, D., Zhang, M., et al. (2016). Interfacial modification layers based on carbon dots for efficient inverted polymer solar cells exceeding 10% power conversion efficiency. *Nano Energy* 26, 216–223. <https://doi.org/10.1016/j.nanoen.2016.05.011>.
 25. Shankar, P., Ishak, M.H., Padarti, J.K., Mintcheva, N., Iwamori, S., Gurbatov, S.O., Lee, J.H., and Kulnich, S.A. (2020). ZnO@graphene oxide core@shell nanoparticles prepared via one-pot approach based on laser ablation in water. *Appl. Surf. Sci.* 531, 147365. <https://doi.org/10.1016/j.apsusc.2020.147365>.
 26. Wang, Y., Yan, L., Ji, G., Wang, C., Gu, H., Luo, Q., Chen, Q., Chen, L., Yang, Y., Ma, C.Q., and Liu, X. (2019). Synthesis of N,S-doped carbon quantum dots for use in organic solar cells as the ZnO modifier to eliminate the light-soaking effect. *ACS Appl. Mater. Interfaces* 11, 2243–2253. <https://doi.org/10.1021/acsami.8b17128>.
 27. Jadoun, S., Riaz, U., Yáñez, J., and Pal Singh Chauhan, N. (2021). Synthesis, characterization and potential applications of poly(o-phenylenediamine) based copolymers and nanocomposites: a comprehensive review. *Eur. Polym. J.* 156, 110600. <https://doi.org/10.1016/j.eurpolymj.2021.110600>.
 28. Beek, W.J.E., Wienk, M.M., Kemerink, M., Yang, X., and Janssen, R.A.J. (2005). Hybrid zinc oxide conjugated polymer bulk heterojunction solar cells. *J. Phys. Chem. B* 109, 9505–9516. <https://doi.org/10.1021/jp050745x>.
 29. Wang, J., Wang, Z., Huang, B., Ma, Y., Liu, Y., Qin, X., Zhang, X., and Dai, Y. (2012). Oxygen vacancy induced band-gap narrowing and enhanced visible light photocatalytic activity of ZnO. *ACS Appl. Mater. Interfaces* 4, 4024–4030. <https://doi.org/10.1021/am300835p>.
 30. Spanhel, L., and Anderson, M.A. (1991). Semiconductor clusters in the sol-gel process: quantized aggregation, gelation, and crystal growth in concentrated zinc oxide colloids. *J. Am. Chem. Soc.* 113, 2826–2833. <https://doi.org/10.1021/ja00008a004>.
 31. Wang, C., Luo, D., Gao, Y., Wang, G., Wang, C., Ma, P., Li, H., Wen, S., Dong, W., and Ruan, S. (2019). Delicate energy-level adjustment and interfacial defect passivation of ZnO electron transport layers in organic solar cells by constructing ZnO/In nanojunctions. *J. Phys. Chem. C* 123, 16546–16555. <https://doi.org/10.1021/acs.jpcc.9b03776>.
 32. Sharma, R., Alam, F., Sharma, A.K., Dutta, V., and Dhawan, S.K. (2014). ZnO anchored graphene hydrophobic nanocomposite-based bulk heterojunction solar cells showing enhanced short-circuit current. *J. Mater. Chem. C* 2, 8142–8151. <https://doi.org/10.1039/c4tc01056f>.
 33. Hillman, F., and Jeong, H.K. (2019). Linker-doped zeolitic imidazolate frameworks (ZIFs) and their ultrathin membranes for tunable gas separations. *ACS Appl. Mater. Interfaces* 11, 18377–18385. <https://doi.org/10.1021/acsami.9b02114>.
 34. Zhang, X., Li, G., Wang, J., Chu, J., Wang, F., Hu, Z., and Song, Z. (2022). Revisiting the structure and electrochemical performance of poly(o-phenylenediamine) as an organic cathode material. *ACS Appl. Mater. Interfaces* 14, 27968–27978. <https://doi.org/10.1021/acsami.2c06208>.
 35. Yang, C., Dong, W., Cui, G., Zhao, Y., Shi, X., Xia, X., Tang, B., and Wang, W. (2017). Highly-efficient photocatalytic degradation of methylene blue by PoPD-modified TiO₂ nanocomposites due to photosensitization-synergetic effect of TiO₂ with PoPD. *Sci. Rep.* 7, 3973. <https://doi.org/10.1038/s41598-017-04398-x>.
 36. Zhang, H., Li, W., Qin, G., Fang, L., Ruan, H., Tan, M., Wu, F., and Kong, C. (2018). Effect of surface carbon contamination on the chemical states of N-doped ZnO thin films. *Appl. Phys.* 124, 147. <https://doi.org/10.1007/s00339-018-1565-x>.
 37. Polydorou, E., Sakellis, I., Soutlati, A., Kaltzoglou, A., Papadopoulos, T.A., Briscoe, J., Tsikritzis, D., Fakis, M., Palilis, L.C., Kennou, S., et al. (2017). Avoiding ambient air and light induced degradation in high-efficiency polymer solar cells by the use of hydrogen-doped zinc oxide as electron extraction material. *Nano Energy* 34, 500–514. <https://doi.org/10.1016/j.nanoen.2017.02.047>.
 38. Chen, M., Wang, X., Yu, Y., Pei, Z., Bai, X., Sun, C., Huang, R., and Wen, L. (2000). X-ray photoelectron spectroscopy and auger electron spectroscopy studies of Al-doped ZnO films. *Appl. Surf. Sci.* 158, 134–140. [https://doi.org/10.1016/S0169-4332\(99\)00601-7](https://doi.org/10.1016/S0169-4332(99)00601-7).
 39. Mohammed, S.M., Shehab, W.S., Emwas, A.H.M., Jaremko, M., Abdellatif, M.H., Zordok, W.A., and Tantawy, E.S. (2023). Eco-Friendly Synthesis of a1 H-benzo[d]imidazole Derivatives by ZnO NPs Characterization, DFT Studies, Antioxidant and Insilico Studies. *Pharmaceuticals* 16, 969. <https://doi.org/10.3390/ph16070969>.
 40. Jiang, K., Sun, S., Zhang, L., Lu, Y., Wu, A., Cai, C., and Lin, H. (2015). Red, green, and blue luminescence by carbon dots: full-color emission tuning and multicolor cellular imaging. *Angew. Chem.* 127, 5450–5453. <https://doi.org/10.1002/ange.201501193>.
 41. Guo, M.Y., Ng, A.M.C., Liu, F., Djurišić, A.B., Chan, W.K., Su, H., and Wong, K.S. (2011). Effect of native defects on photocatalytic properties of ZnO. *J. Phys. Chem. C* 115, 11095–11101. <https://doi.org/10.1021/jp200926u>.
 42. Hannachi, E., Slimani, Y., Nawaz, M., Sivakumar, R., Trabelsi, Z., Vignesh, R., Akhtar, S., Almessiere, M.A., Baykal, A., and Yasin, G. (2023). Preparation of cerium and yttrium doped ZnO nanoparticles and tracking their structural, optical, and photocatalytic performances. *J. Rare Earths* 41, 682–688. <https://doi.org/10.1016/j.jre.2022.03.020>.
 43. Yuan, J., Zhang, Y., Zhou, L., Zhang, G., Yip, H.L., Lau, T.K., Lu, X., Zhu, C., Peng, H., Johnson, P.A., et al. (2019). Single-junction organic solar cell with over 15% efficiency using fused-ring acceptor with electron-deficient core. *Joule* 3, 1140–1151. <https://doi.org/10.1016/j.joule.2019.01.004>.
 44. Chen, G., Wang, T., Li, C., Yang, L., Xu, T., Zhu, W., Gao, Y., and Wei, B. (2016). Enhanced photovoltaic performance in inverted polymer solar cells using Li ion doped ZnO cathode buffer layer. *Org. Electron.* 36, 50–56. <https://doi.org/10.1016/j.orgel.2016.05.033>.
 45. Höfle, S., Schienle, A., Bruns, M., Lemmer, U., and Colmann, A. (2014). Enhanced electron injection into inverted polymer light-emitting diodes by combined solution-processed zinc oxide/polyethylenimine interlayers. *Adv. Mater.* 26, 2750–2754. <https://doi.org/10.1002/adma.201304666>.
 46. Qi, B., and Wang, J. (2013). Fill factor in organic solar cells. *Phys. Chem. Chem. Phys.* 15, 8972–8982. <https://doi.org/10.1039/C3CP51383A>.
 47. Zhang, H., Stubhan, T., Li, N., Turbiez, M., Matt, G.J., Ameri, T., and Brabec, C.J. (2014). A solution-processed barium hydroxide modified aluminum doped zinc oxide layer for highly efficient inverted organic solar cells. *J. Mater. Chem. A* 2, 18917–18923. <https://doi.org/10.1039/C4TA03421J>.
 48. Lee, J.H., Cho, S., Roy, A., Jung, H.T., and Heeger, A.J. (2010). Enhanced diode characteristics of organic solar cells using titanium suboxide electron transport layer. *Appl. Phys. Lett.* 96, 163303. <https://doi.org/10.1063/1.3409116>.
 49. Yang, Y., Guo, W., Wang, X., Wang, Z., Qi, J., and Zhang, Y. (2012). Size dependence of dielectric constant in a single pencil-like ZnO nanowire. *Nano Lett.* 12, 1919–1922. <https://doi.org/10.1021/nl204353t>.

50. Kumar, S.G., and Rao, K.S.R.K. (2015). Zinc oxide based photocatalysis: tailoring surface-bulk structure and related interfacial charge carrier dynamics for better environmental applications. *RSC Adv.* 5, 3306–3351. <https://doi.org/10.1039/C4RA13299H>.
51. Lin, C., Hsieh, C., Macdonald, T.J., Chang, J., Lin, P., Cha, H., Steier, L., Wadsworth, A., McCulloch, I., Chueh, C., and Durrant, J.R. (2022). Water-insensitive electron transport and photoactive layers for improved underwater stability of organic photovoltaics. *Adv. Funct. Mater.* 32, 2203487. <https://doi.org/10.1002/adfm.202203487>.
52. Liu, B., Han, Y., Li, Z., Gu, H., Yan, L., Lin, Y., Luo, Q., Yang, S., and Ma, C.Q. (2020). Visible light-induced degradation of inverted polymer:nonfullerene acceptor solar cells: initiated by the light absorption of ZnO layer. *Sol. RRL* 5, 2000638. <https://doi.org/10.1002/solr.202000638>.
53. Hu, L., Jiang, Y., Sun, L., Xie, C., Qin, F., Wang, W., and Zhou, Y. (2021). Significant enhancement of illumination stability of nonfullerene organic solar cells via an aqueous polyethylenimine modification. *J. Phys. Chem. Lett.* 12, 2607–2614. <https://doi.org/10.1021/acs.jpclett.1c00276>.
54. Liu, B., Su, X., Lin, Y., Li, Z., Yan, L., Han, Y., Luo, Q., Fang, J., Yang, S., Tan, H., and Ma, C.Q. (2022). Simultaneously achieving highly efficient and stable polymer:non-fullerene solar cells enabled by molecular structure optimization and surface passivation. *Adv. Sci.* 9, 2104588. <https://doi.org/10.1002/advs.202104588>.
55. Perdew, J., Burke, K., and Ernzerhof, M. (1996). Generalized gradient approximation made simple. *Phys. Rev. Lett.* 77, 3865–3868. <https://doi.org/10.1103/PhysRevLett.77.3865>.
56. Kresse, G., and Furthmüller, J. (1996). Efficiency of ab-initio total energy calculations for metals and semiconductors using a plane-wave basis set. *Comput. Mater. Sci.* 6, 15–50. [https://doi.org/10.1016/0927-0256\(96\)00008-0](https://doi.org/10.1016/0927-0256(96)00008-0).
57. Kresse, G., and Furthmüller, J. (1996). Efficient iterative schemes for ab-initio total-energy calculations using a plane-wave basis set. *Phys. Rev. B* 54, 11169–11186. <https://doi.org/10.1103/PhysRevB.54.11169>.
58. Kresse, G., and Joubert, D. (1999). From ultrasoft pseudopotentials to the projector augmented-wave method. *Phys. Rev. B* 59, 1758–1775. <https://doi.org/10.1103/PhysRevB.59.1758>.
59. Blöchl, P. (1994). Projector augmented-wave method. *Phys. Rev. B* 50, 17953–17979. <https://doi.org/10.1103/PhysRevB.50.17953>.
60. Monkhorst, H.J., and Pack, J.D. (1976). Special points for brillouin-zone integrations. *Phys. Rev. B* 13, 5188–5192. <https://doi.org/10.1103/PhysRevB.13.5188>.
61. Grimme, S., Antony, J., Ehrlich, S., and Krieg, H. (2010). A consistent and accurate ab-initio parametrization of density functional dispersion correction (DFT-D) for the 94 elements H-Pu. *J. Chem. Phys.* 132, 154104. <https://doi.org/10.1063/1.3382344>.
62. Grimme, S., Ehrlich, S., and Goerigk, L. (2011). Effect of the damping function in dispersion corrected density functional theory. *J. Comput. Chem.* 32, 1456–1465. <https://doi.org/10.1002/jcc.21759>.